

# International Conference on Space Optics—ICSO 2012

Ajaccio, Corse

9–12 October 2012

*Edited by Bruno Cugny, Errico Armandillo, and Nikos Karafolas*



## *Final results of the PERSEE experiment*

*J.-M. Le Duigou*

*J. Lozi*

*F. Cassaing*

*K. Houairi*

*et al.*



## Final results of the PERSEE experiment

J.M. Le Duigou<sup>1</sup>, J. Lozi<sup>2,7</sup>, F. Cassaing<sup>2,7</sup>, K. Houairi<sup>2,7</sup>, B. Sorrente<sup>2,7</sup>, J. Montri<sup>2,7</sup>, S. Jacquinod<sup>3</sup>, J.M. Reess<sup>4,7</sup>, L. Pham<sup>4,7</sup>, E. Lhome<sup>4,7</sup>, T. Buey<sup>4</sup>, F. Hénault<sup>5</sup>, A. Marcotto<sup>5</sup>, P. Girard<sup>5</sup>, N. Mauclert<sup>5</sup>, M. Barillot<sup>6</sup>, V. Coudé du Foresto<sup>4</sup>, M. Ollivier<sup>3</sup>

<sup>1</sup>: Centre National d'Etudes Spatiale  
18 Avenue Edouard Belin  
31401 TOULOUSE Cedex 9 – France  
Tel: (+33) 1 61 28 21 24  
Fax: (+33) 1 61 28 26 92

[Jean-Michel.LeDuigou@cnes.fr](mailto:Jean-Michel.LeDuigou@cnes.fr)

<sup>2</sup>: Office National d'Etudes et de Recherches Aérospatiales

<sup>3</sup>: Institut d'Astrophysique Spatiale d'Orsay

<sup>4</sup>: Observatoire de Paris

<sup>5</sup>: Observatoire de la Côte d'Azur

<sup>6</sup>: Thalès Alénia Space

<sup>7</sup>: Groupement d'Intérêt Scientifique PHASE (Partenariat Haute résolution Angulaire Sol Espace)

**ABSTRACT:** The PERSEE breadboard, developed by a consortium including CNES, IAS, LESIA, OCA, ONERA and TAS since 2006, is a nulling demonstrator that couples an infrared nulling interferometer with a formation flying simulator able to introduce realistic disturbances in the set-up. The general idea is to prove that an adequate optical design can considerably release the constraints applied at the spacecrafts level of a future interferometric space mission like Darwin/TPF or one of its precursors. The breadboard is now fully operational and the measurements sequences are managed from a remote control room using automatic procedures. A set of excellent results were obtained in 2011: the measured polychromatic nulling depth with non polarized light is  $8.8 \times 10^{-6}$  stabilized at  $9 \times 10^{-8}$  in the  $[1.65-2.45] \mu\text{m}$  spectral band (37% bandwidth) during 100s. This result was extended to a 7h duration thanks to an automatic calibration process. The various contributors are identified and the nulling budget is now well mastered. We also proved that harmonic disturbances in the 1-100Hz up to several tens of nm rms can be very efficiently corrected by a Linear Quadratic Control (LQG) if a sufficient flux is available. These results are important contributions to the feasibility of a future space based nulling interferometer.

**Keywords:** Interferometry, Formation flying, Nulling, exoplanets, Darwin, TPF, Pegase.

### 1. INTRODUCTION

Although it has been recently postponed due to high cost and risks, nulling interferometry in space remains one of the very few direct detection methods able to characterize extrasolar planets and particularly telluric ones. Within this framework, several projects such as DARWIN [1], [2], TPF-I [3], [4], FKSII [5] or PEGASE [6], [7], have been proposed in the past years. Most of them are based on a free flying concept. It allows firstly avoiding atmosphere turbulence, and secondly distributing instrumental function over many satellites flying in close formation. In this way, a very high angular resolution can be achieved with an acceptable launch mass. But the price to pay is to very precisely position and relatively stabilize the spacecrafts, in order to achieve a deep and stable extinction of the star. Understanding and mastering all these requirements are great challenges and key issues towards the feasibility of these missions. Thus, we decided to experimentally study this question and focus on some possible simplifications of the concept.

Since 2006, PERSEE (PEGASE Experiment for Research and Stabilization of Extreme Extinction) laboratory test bench is under development by a consortium composed of Centre National d'Etudes Spatiales (CNES), Institut d'Astrophysique Spatiale (IAS), Observatoire de Paris (LESIA), Observatoire de la Côte d'Azur (OCA), Office National d'Etudes et de Recherches Aérospatiales (ONERA), and Thalès Alénia Space (TAS). It is mainly funded by CNES R&D. PERSEE couples an infrared wide-band nulling interferometer with local OPD and tip/tilt control loops and a perturbation system able to introduce realistic disturbances in the set-up. Although it was designed in the framework of the PEGASE free flying space mission, PERSEE can adapt very easily to

other contexts like FKSI (in space, with a 10m long beam structure) or ALADDIN [8] (on ground, in Antarctica) because the optical designs of all those missions are very similar. After a short description of the experimental setup, we will present the experimental results of the cophasing systems and the measured polychromatic nulling ratio. A detailed analysis of the nulling budget is also presented based on various experiments performed on PERSEE.

## 2. DESCRIPTION OF PERSEE

This section provides the reader with a brief description of PERSEE. More details can be obtained by the interested reader from [9] - [12].

### 2.1. Goals

Starting from a state-of-the-art nuller of the 2006-2007 period, PERSEE is an experimental attempt to better master the system flowdown of the nulling requirements both at payload (instrument main optical bench) and platform levels (satellites). The balance of the constraints between those two levels is a key issue. The more disturbances the payload can face, the simpler the platforms, the lower the cost. The general idea is hence to simplify as much as possible the global design and reduce the costs of a possible future space mission. Our main requirement is to reach a  $10^{-4}$  nulling ratio in the  $[1.65-2.4] \mu\text{m}$  band (about 40% spectral bandwidth) with a  $10^{-5}$  stability over a 10h time scale despite the injection of representative disturbances. Another important requirement is to be able to find and stabilize fringes, which have an initial drift speed (as seen from the interferometer core) up to  $150 \mu\text{m/s}$ , as this can greatly simplify the relative metrology and control needs. We want to study and maximize the rejection of external disturbances introduced at relevant degrees of freedom of the optical setup by a disturbance module simulating various environments coming from the satellite level.

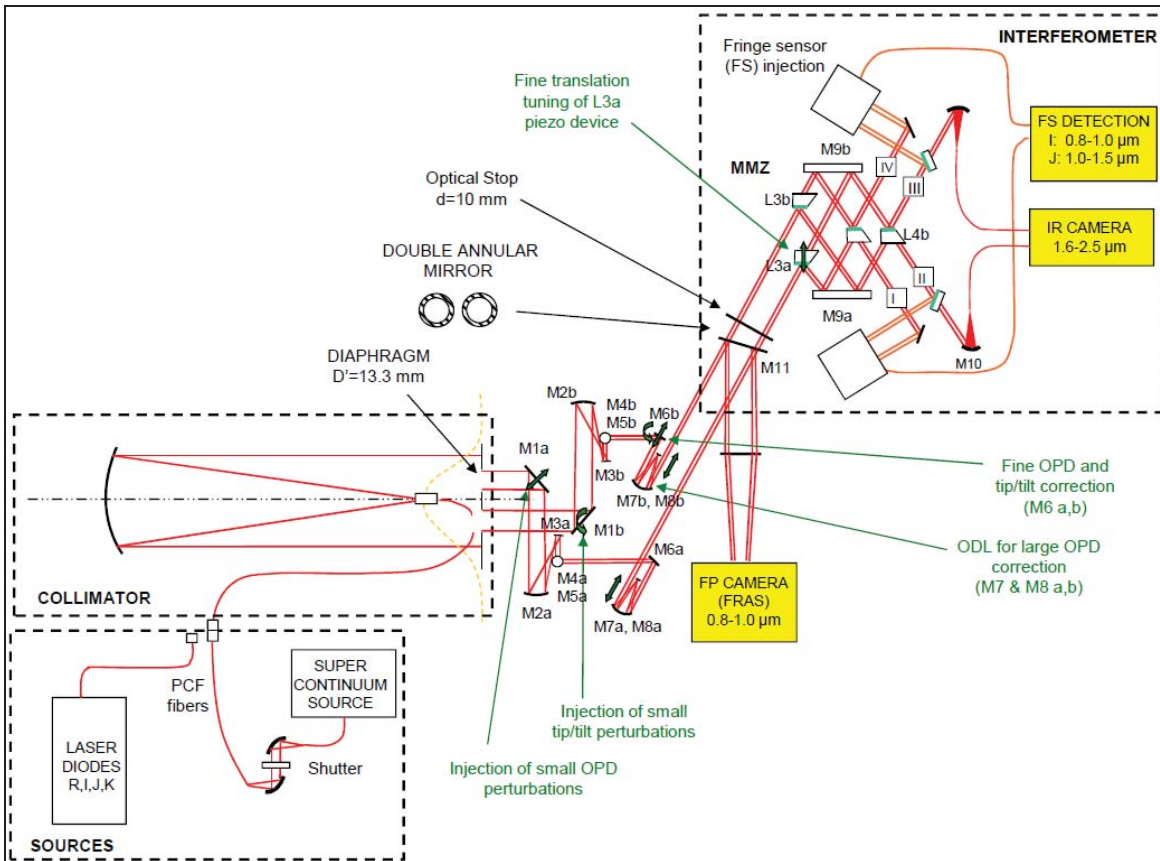


Fig. 1: general setup of PERSEE in its final operational state.

### 2.2. Optical setup

Fig. 1 gives an overview of the up-dated optical layout. Part of the real implementation of the PERSEE is illustrated by fig. 2. With respect to earlier versions, the source module was changed. It finally uses a super-continuum high power laser source covering a wide spectral range from  $[0.6-2.5] \mu\text{m}$  instead of three

separate sources. The light is injected at the focus of a 750mm collimator through a PCF (Photonic Crystal Fiber) fiber designed to be single mode in the full spectral range, but with a chromatic numerical aperture. The R sub-band ( $[0.6-0.8] \mu\text{m}$ ) is used for alignment purposes. The I sub-band ( $[0.8-1] \mu\text{m}$ ) is dedicated to the channel 1 of the Fringe Sensor (FS) and the Field Relative Angle Sensor (FRAS). The J sub-band ( $[1-1.5] \mu\text{m}$ ) is dedicated to the channel 2 of the FS. The nulling rate is measured in the H+K band ( $[1.65-2.5] \mu\text{m}$ ). The two 40mm beams (a and b) coming out of the separation module first encounter two  $45^\circ$  fold mirrors (M1) simulating the siderostats of PEGASE [6], [7]. Accurately calibrated perturbations can be introduced at this level either in tip/tilt (few tens of mas resolution) or OPD (nm resolution). In the full design presented below, the optical train incorporates afocal systems with  $M=3$  magnification to reduce the beam size down to about 13mm, which is a feasible size for the combination part. These devices were needed first to simulate the possible effects of this optical function ( $M=20$  to  $M=40$  in PEGASE) then to get enough photons with the original source design, which used a much weaker source in the K band. As the source was changed to a more powerful one, the second reason to implement the afocals is no more valid. All presented results were made without the afocals, directly taking a 13 mm pupil from the collimator to the M1 mirror. The study of their possible effect on the performance is postponed to a later step as this is supposed to be a second order contributor.

The M4 mirrors deviate the beam toward the  $-Z$  direction. Coupled with the M1 mirrors, they create a “field reversal” Achromatic Phase Shift (APS) between the two arms. This is the most efficient way to implement this optical function as it doesn't require additional dispersive optical parts. Following, each arm has a cat's eye Optical Delay Line (ODL, 50mm stroke and 10nm resolution) and a  $30^\circ$  active M6 mirror acting both in tip/tilt and fine OPD ( $12\mu\text{m}$  or 240 arcsec stroke, 0.2nm resolution). These active systems can all together generate various corrections covering the necessary range and resolution both in tip/tilt and OPD. They are used in dedicated control loops, which use the FRAS camera for the tip/tilt and the FS for the OPD. The optical stop is placed after the ODL. The design of the ODL (second mirror curvature) is made to optically conjugate the stop and the M6 mirrors. In this way, the coupling between the OPD and tip/tilt degrees of freedom is minimized. L1 and L2, located just before the combination stage, are an optional chromatism compensator, which was finally not used due to the excellent quality of the MMZ (Modified Mach-Zehnder) manufacturing.

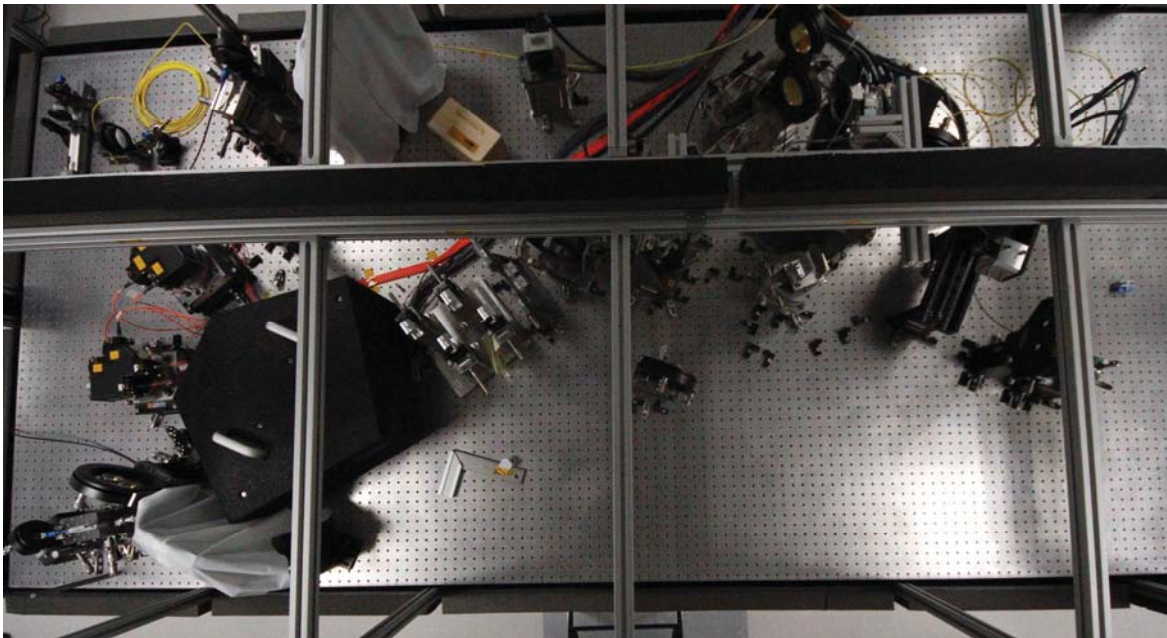


**Fig. 2:** top view of the real implementation, optical train and MMZ (the source module source and the camera are implemented on separate optical tables).

The combination stage is a kind of Modified Mach-Zehnder (MMZ) [14] with two inputs (a and b arms) and four outputs (I to IV). Due to some symmetry and optical tight tolerances (geometry and coatings), the setup guarantees that two outputs are achromatic. The four beam splitters have a trapezoidal geometry [13] to avoid stray light. They have a specifically designed three-layer coating of about 200nm thickness, which allows achieving appropriate reflection and transmission coefficients for both polarizations in the whole H+K band. The beam splitters are divided into two groups as compared to the classical setup. This allows translating the L3a component without impacting the nulling output (output III). The translation is adjusted so that the four outputs generate four points in the I and J fringes roughly with a  $\lambda/4$  spacing, which allows a spatial ABCD-type fringe

tracking algorithm. The tip/tilt degrees of freedom of L3a are used to maximize the contrast in the FS I and IV outputs. This compact design allows minimizing differential optical path between FS and nulled output down to about 10cm. This point is critical because it releases the stabilization requirements at system level.

After the MMZ, dichroic plates separate the various spectral channels and direct them into appropriate detection chains via injection into optical fibers. The FS detection is made of a set of eight monopixels and multimode fibers. The chromatism of the injection lenses makes the FS spectral bands sensitive to the alignment of these lenses. For the K channel, the light is injected in a fluoride glass single mode fiber. The detector is a nitrogen cooled infrared camera based on a Teledyne PICNIC matrix behind a dispersive element, which allows having polychromatic measurements of both dark and bright fringes at the same time. A calibrated optical attenuator is used in the bright output to optimize the dynamic range of both outputs with respect to the detector well depth.

### 3. EXPERIMENTAL RESULTS OF THE COPHASING SYSTEM

#### 3.1 Tip/tilt under laboratory environment

The tip/tilt of each arm for the science channel is optimized to maximize the coupling into the single mode fiber of the nulled output (III). At the beginning of each measurement sequence, a calibration procedure [16] is performed to find the reference position for each arm. Then a control loop maintains the position around this reference. This loop is based on the M6 mirrors, the FRAS camera and a classical integrator as the control law. The

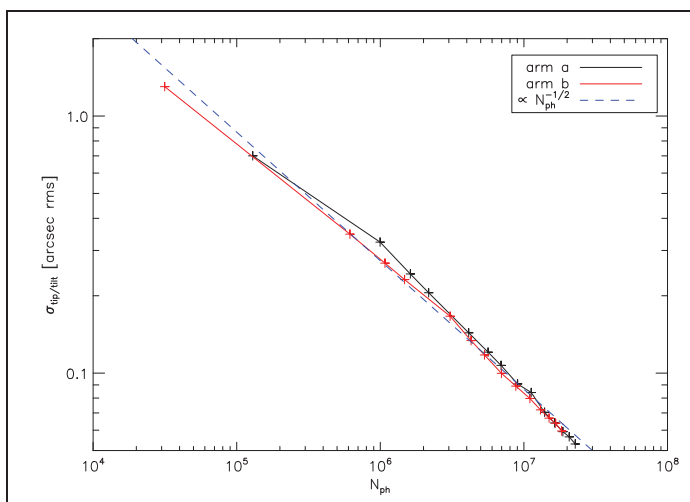


Fig. 4: tip/tilt noise as function of flux (closed loop).

As the contributors beyond 5Hz are very low, the gain of the closed loop can be set to a low value (0.05). The maximum cutting frequency is about 10Hz. Using the maximum flux of the source, the closed loop performance obtained is 56mas rms, about 1/100<sup>th</sup> of the pixel size (6 arcsec). Fig 4 shows the decrease of this performance with the photon count. As expected, we find a  $N^{-1/2}$  slope, which shows that our set-up is photon-noise limited as expected. The initial requirement of 600mas can be reached for  $2 \times 10^5$  ADU (total for the image of the point source in one arm, including the optical transmission and the quantum efficiency of the detector).

#### 3.2 OPD under laboratory environment

The OPD is much more sensitive to mechanical disturbances coming either from the laboratory or from a calibrated disturbance. During the step-by-step integration progress, the various vibrations coming from the environment were characterized. In the most favorable case, without transient event (no aircraft flying above the campus, no subway passing underground, nobody closing a door or walking in the nearby rooms...), we measured the PSD of the OPD noise of fig. 5a (black curve), with an overall level of 1.1nm rms. At low frequency, the PSD is dominated by the turbulence. The power supply is responsible for the 50Hz very narrow peak and the associated harmonics. The other broader peaks are due to vibration modes of the optical mounts: ODL (80Hz), MMZ (130Hz to 170Hz), M6 (110Hz), which are excited by low frequency disturbances from the building. The M6 piezo-electric devices have strain-gauges to control their position. They are responsible for an additional noise as can be seen on the black curve as compared to the red one on fig. 5a. The air-conditioning

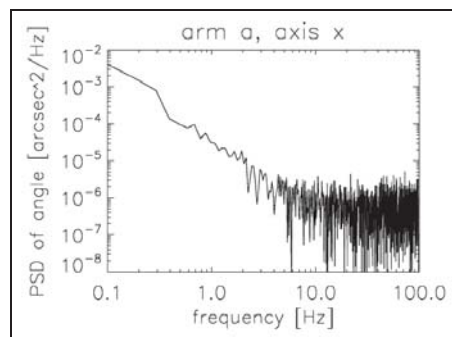


Fig. 3: tip/tilt noise (open loop).

camera measures the flux of an annular section of the beams in the I band. The maximum reading frequency of the camera is 200Hz. The open loop noise is about 500mas and is dominated by the turbulence effect at low frequency as shown on fig. 3. The tip/tilt is not very sensitive to the laboratory disturbances and is easier to control than the OPD. Furthermore, we did not try to inject calibrated perturbations in tip/tilt because this is far less critical than on the OPD.

and over-pressure systems were OFF during this measurement. As the associated machinery is located at the same level of the building, it generates quite high vibrations (5-6nm rms each). They are not compatible with our goals and we had to shut them down during all measurements. The drawback is that we had to perform regular calibrations of the experiment because the temperature slowly drifts.

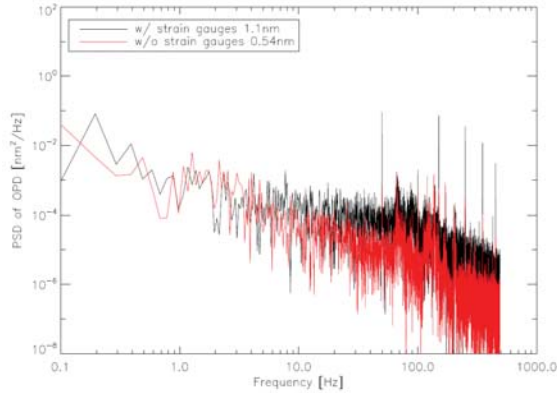


Fig. 5a: OPD residual noise, open loop.

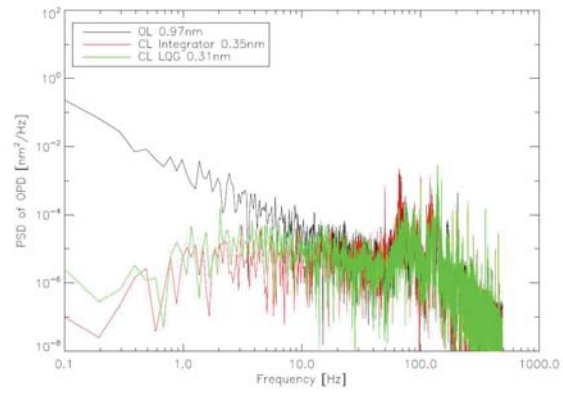


Fig. 5b: closed loop vs to open loop, integrator or LQG.

Two control laws were implemented: a simple integrator or a more complex Linear Quadratic Gaussian (LQG) controller. Details of the LQG implemented in PERSEE can be found in [15]. It uses an *a priori* model of the disturbances structure: a low frequency part corresponding either to the turbulence (ground) or to a residue of the GNC control (space mission), a number of harmonic functions represented by second order systems, and a high frequency measurement noise. Using the open loop measurement, an identification is performed using this model to estimate the various parameters (frequency, damping and level of harmonic functions, level of the noise, low frequency level). This information is then used within a Kalman filtering to optimize the control loop. The performance of this type of control is highly related to the quality of the perturbation model used. When applied to the “natural” environment of the laboratory, both controllers have similar results as the disturbance to correct is very low. The residual OPD noise is reduced down to 0.3-0.35nm rms. Associated with the very good tip/tilt performance, the PERSEE set-up provides excellent conditions for accurate nulling measurements.

### 3.3 OPD under calibrated disturbances

One very important feature of PERSEE is the ability to inject calibrated disturbances simulating a real in-flight environment. Up to now, only the small displacements part is implemented and tested. As the principles are the same for both tip/tilt and OPD, the experimentation was limited to OPD because it is far a more sensitive parameter for the nulling ratio. But the results could easily be translated to the two other degrees of freedom if they were supposed to face important perturbations in flight. From the PEGASE phase 0, we derived various disturbances cases. The GNC is supposed to perform a first control of the satellites relative and absolute positions. The foreseen architecture involves a continuous control on the siderostats with 3 reaction wheels as actuators and a pulsed control on the combiner with an actuation period of about 100s. The GNC damps the relative movement of the satellites and reduces the OPD noise in the control band (1Hz) to an acceptable level for the optical payload [17]. The first contributor to consider is then a low frequency term below 1Hz. In the worst case it was estimated to 3nm rms.

Following, as the reaction wheels are rotating machines with imperfect balance, they generate a harmonic perturbation composed of a fundamental sine function at the wheel speed and various harmonics linked to the geometry of the bearings. In some cases, a coincidence may occur between one of the harmonics of one of the 6 wheels and a structural mode. No detailed model was built, but the following hypothesis were made on base of CNES previous experience in the field of micro vibrations [18]: wheel speed 1Hz, 3.5Hz or 4.5Hz, first solar array mode at 15Hz (they lay on quite rigid sun-shades [7]), first siderostat global mode at 55Hz (300kg quite compact

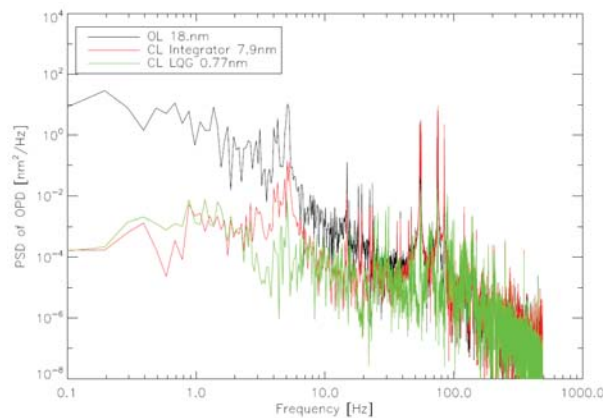


Fig. 6: OPD noise as function of flux (closed loop with integrator or LQG compared to open loop).

satellite), first local mode of M1 mirror assembly at 75Hz, first local mode of the wheels supporting structure at 85Hz. To obtain worst cases, multiple coincidences are allowed. The most conservative case is illustrated by fig. 6. The black curve is the injected perturbation without correction. The overall level is 18nm rms. Both control laws can face the low frequency part efficiently. But only the LQG can significantly reduce the effect of the amplified wheels harmonics and reduce the overall level down to 0.77nm rms.

Systematic tests were performed to test the robustness of the process with respect to the amplitude of each sine function, the frequency separation and the number of harmonics. The LQG performs very well even with a

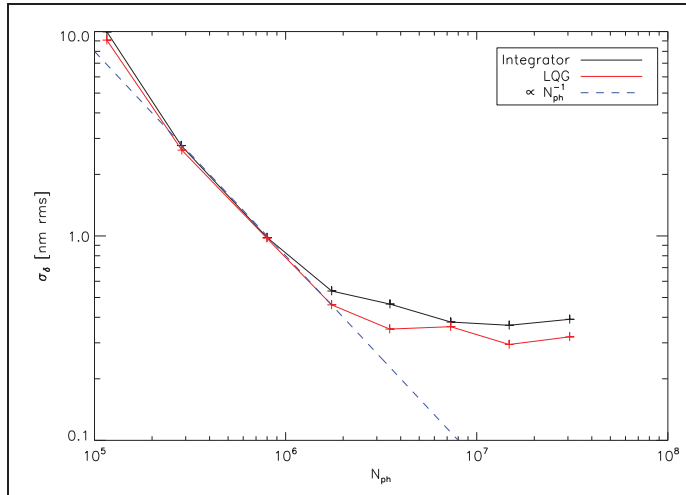


Fig. 7: OPD noise as function of flux (closed loop).

single harmonic up to 100nm, two harmonics as close as 0.1Hz and 20 harmonics of 10nm each. These results are only possible if a high flux is available as this allows a high bandpass (1kHz sampling frequency). This is the case with the super-continuum source on the experimental set-up. When reducing the flux, the measurement noise increases as illustrated by fig. 7.  $N_{ph}$  is the total number of photons detected in the FS I channel (2 arms, 4 outputs, quantum efficiency included). At very low flux, the noise is dominated by the detectors noise, as expected. In the high flux domain, the experimental law is  $N_{ph}^{-1}$  instead of the  $N_{ph}^{-1/2}$  expected one. This is linked to the statistics of the source optical power noise. Its variance is

proportional to the square of the average power. The physical origin comes from the non linear effects in the PCF. In the test set-up, the required performance can be reached for  $3 \times 10^5$  photons in the I band (SNR of 440).

## 4. EXPERIMENTAL NULLING RESULTS

### 4.1 Mathematical background

The extinction ratio is defined as:

$$N(\lambda, t) = I_{\min}(\lambda, t) / I_{\max}(\lambda, t)$$

This quantity can be averaged over a spectral band ( $\langle N \rangle_\lambda$ ) or over a time duration ( $\langle N \rangle_t$ ), or both.  $\sigma$  is used for the associated variance.  $I_{\min}$  and  $I_{\max}$  are the minimum and maximum intensity of a fringe pattern as a function of OPD. The total spectral range is divided into 9 bands ( $i=1$  to 9). A detailed mathematical formulation is derived in [19] and was used as a basis of our nulling budget, but with some extension to take into account the spectral analysis. An important point is that the OPD cannot be optimized to minimize the extinction ratio of all spectral bands simultaneously. The ideal position is  $OPD=0$ , but due to imperfect calibration between the FS and the nulled output, the FS reference position has to be set to a value  $\delta_{ref}$ , which is not zero but experimentally minimizes the average extinction rate on the whole band. This reference position is sensitive to temperature changes and has to be calibrated regularly. This is related to the thermo-elastic non stability of the non-common optical paths in the MMZ. Let  $\delta_i$  be the OPD offset with respect to  $\delta_{ref}$ , which minimizes the extinction ratio for the I band and  $\lambda_i$  its central wavelength.  $\delta_i$  and  $\lambda_i$  are measured during the calibration process [16]. The intensity of arm a or b coupled into the single mode fiber writes:

$$I_{a \text{ or } b, I} = I_{a \text{ or } b, I_{\max}} [1 - 1/5 (\pi D \theta_{a \text{ or } b}(t) / \lambda_i)^2]$$

$I_{a \text{ or } b, I_{\max}}$  is the maximal intensity coupled into the fiber obtained for the tip/tilt reference position  $(\alpha, \beta)_{a \text{ or } b, ref}$  during the tip/tilt calibration process.  $\theta_{a \text{ or } b}(t)$  is the difference between the tip/tilt current position and this reference position (norm of  $(\alpha, \beta)$ ). It is the residual noise of the tip/tilt control loop.  $D=10$  mm is the diameter of the collimated beam before injection into the fiber.

The main contributors of the time averaged extinction ratio in the I band are:

- OPD

- chromatism main term  $(\pi\delta_i/\lambda_i)^2$
- OPD noise  $(\pi\sigma_\delta/\lambda_i)^2$  where  $\sigma_\delta$  is the OPD noise as measured on the FS
- coupling term  $(\pi/\lambda_i)^2 (\delta_{ref}^2 + 2 \delta_i \delta_{ref})$
  
- Intensity mismatch
  - quasi-static term  $\epsilon_{i,stat}^2/4$ , where  $\epsilon_{i,stat} = (I_{b,i} - I_{a,i}) / (I_{b,i} + I_{a,i})$
  - noise  $1/400 (\pi D/\lambda_i)^2 [\theta_b(t)^2 - \theta_a(t)^2]$
- Polarization
  - rotation  $\alpha_{i,rot}^2/4$ , where  $\alpha_{rot}$  is the differential rotation angle of the polarization between arm a and b as measured in I band
  - s-p delay  $\alpha_{i,s-p}^2/4$ , where  $\alpha_{s-p}$  is the differential delay between s and p polarization state

**4.2 Monochromatic light**

The results in the monochromatic case are presented in [20]. They were performed on an intermediate configuration limited to the MMZ used in an auto-collimation set-up with laser diodes injected from the outputs of the set-up and reflected back by the M6 positioned at the entrance of the MMZ. The best obtained nulling ratio over a 100s duration is  $5.6 \times 10^{-6}$  (temporal average over 100s). The OPD contribution accounts only for  $3 \times 10^{-7}$ . Many effects due to the imperfect calibration limited the performances. Each of them was addressed before proceeding to the polychromatic measurement.

In the monochromatic configuration, the sensitivity of the MMZ to temperature variations could be measured. The dephasing between outputs III and IV is a good indicator of the differential path between the nulling output in H+K band and the FS channels in the I and J bands. It proved to be perfectly correlated to the temperature variations as measured on the MMZ. The measured coefficient is  $1200 \text{nm}/^\circ\text{C}$ . The value for the final configuration is twice less,  $600 \text{nm}/^\circ\text{C}$  (one way only). This high sensitivity comes directly from the standard mounts used for the MMZ and also from the stability of the mechanism under the L3b beam splitter. A much more stable structure with much less adjustable degrees of freedom was planned, but was too costly for the project. Our estimation is that with an appropriate design, the thermal sensitivity of the differential OPD could be reduced by at least a factor of ten.

**4.3 Some calibrations aspects**

**Spectral calibration**

The quantities  $\lambda_i$  and  $\Delta\lambda_i$  for each spectral channel were measured using a Fourier transform analysis. They depend on the FS injection lens chromatic properties and a calibration is required.  $\Delta\lambda_i/\lambda_i$  ranges from 7% to 11%. The total spectral width is defined as:

$$\frac{\Delta\lambda_{moy}}{\lambda_{moy}} = \frac{(\lambda_9 + \Delta\lambda_9 / 2) - (\lambda_1 - \Delta\lambda_1 / 2)}{\lambda_{moy}} = 37\% \text{ with } \lambda_{moy} = 2.0 \mu\text{m}$$

***I<sub>max</sub> measurement***

$I_{min}$  is measured on the output III when the OPD is 0. The flux is dispersed on a 9x2 pixel zone of the PICNIC detector.  $I_{max}$  is the intensity we would have on the central fringe without the  $\pi$  phase shift. As the optical source has power variations of about 10%,  $I_{max}$  has to be measured at the same time as  $I_{min}$  to have accurate results. Furthermore, as  $I_{max}$  is at least  $10^4$  greater than  $I_{min}$ , we used an optical attenuator in the bright output to match the dynamic range of the IR camera. In the original design,  $I_{max}$  was supposed to be measured on the output II of the MMZ using an optical attenuator (second 9x2 pixel zone on the camera). But due to the absorption coefficient of the coatings in the MMZ, the output II is not a fully constructive fringe when output III is a destructive one. There is a phase shift of about  $-20^\circ$ . Hence  $I_{max}$  is sensitive to OPD variations and is not constant in time. Furthermore, getting an excellent coupling ratio in both single mode fibers generates very stringent alignment constraints on the optical set-up. That's why we decided to use another reference. An unused portion of the output pupil of the collimator is measured at the same time as  $I_{min}$  measurement. This  $I_{ref}$  is proportional to  $I_{max}$ . The coefficient is measured through the calibration process.

**4.4 Polychromatic light**

**Results over 100s under the laboratory environment**

The best measurements obtained under the laboratory "natural" environment with the LQG based control on the OPD and the integrator control laws on the tip/tilt are illustrated by fig. 8a and 8b. The left graph is the temporal

evolution over 100s of the spectrally averaged extinction ratio. The black curve is the raw measurement with a reading frequency of the camera of 100Hz and a  $\tau=2.58\text{ms}$  integration time. The green is the convolution with a 1s window. We finally measure:

$$\langle\langle N \rangle\rangle_{\lambda=1.9}^{T=100\text{s}} = 8.8 \times 10^{-6} \text{ with the associated variance } \sigma_{\tau=2.58 \text{ ms}} = 1.5 \times 10^{-6}$$

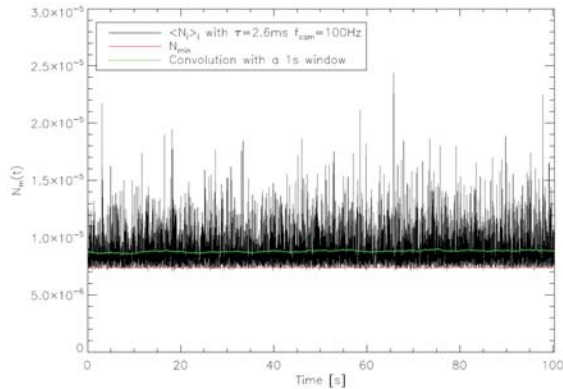


**Fig. 8a:** spectrally averaged null as a function of time.

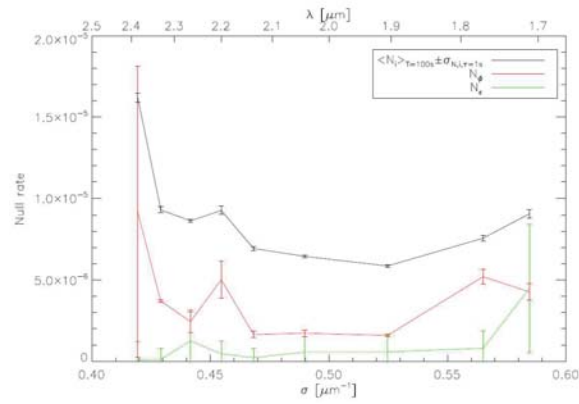


**Fig. 8b:** time averaged extinction ratio in each spectral channel.

Reducing the frequency band by a convolution with a 1s window reduces the variance to  $\sigma_{\tau=1 \text{ s}} = 9 \times 10^{-8}$ . The black curve is the temporal average of the extinction ratio as a function of wavelength (or wave number). It shows that the set-up has very low chromatism effects. The last spectral channel has a degradation of the nulling extinction mainly due to a poorer SNR. It comes from the upper limit of the source spectrum, which is  $2.4\mu\text{m}$ . The red curve is the sum of the OPD effects. Each one was estimated separately, using the FS data for the OPD noise (0.74nm rms noise), the chromatism measured during the calibration, the estimation of  $\delta_{\text{ref}}$  by a statistical analysis of the data. The green one is the sum of the intensity mismatch effects, which were estimated from the FRAS measurement (65mas rms noise). The spectral averaging of this data and a very detailed analysis of the various contributors lead to table 1a, which compares the experimental average nulling budget with the allocations.

$\langle N_{\text{moy}} \rangle_{T=100\text{s}}$	$10^{-4}$	$8,8 \times 10^{-6}$	$\langle N_{\text{moy}} \rangle_{T=7\text{h}}$	$10^{-4}$	$1,02 \times 10^{-5}$
$\langle N_{\phi} \rangle_{T=100\text{s}}$	$7 \times 10^{-5}$	$3,9 \times 10^{-6}$	$\langle N_{\phi} \rangle_{T=7\text{h}}$	$7 \times 10^{-5}$	$4,6 \times 10^{-6}$
$\langle N_{\delta,w} \rangle_{T=100\text{s}}$	} $3,5 \times 10^{-5}$	$1,4 \times 10^{-6}$	$\langle N_{\delta,w} \rangle_{T=7\text{h}}$	} $3,5 \times 10^{-5}$	$1,4 \times 10^{-6}$
$\langle N_{\delta,\text{ref}} \rangle_{T=100\text{s}}$		$10^{-7}$	$\langle N_{\delta,\text{ref}} \rangle_{T=100\text{s}}$		$9,1 \times 10^{-7}$
$N_{\sigma}$	$3,5 \times 10^{-5}$	$2,4 \times 10^{-6}$	$N_{\sigma}$	$3,5 \times 10^{-5}$	$2,3 \times 10^{-6}$
$\langle N_{\epsilon} \rangle_{T=100\text{s}}$	$2 \times 10^{-5}$	$9,5 \times 10^{-7}$	$\langle N_{\epsilon} \rangle_{T=100\text{s}}$	$2 \times 10^{-5}$	$5,5 \times 10^{-7}$
$N_{\epsilon,\text{stat}}$	} $2 \times 10^{-5}$	$9,5 \times 10^{-7}$	$N_{\epsilon,\text{stat}}$	} $2 \times 10^{-5}$	$5,5 \times 10^{-7}$
$\langle N_{\epsilon,\text{dyn}} \rangle_{T=100\text{s}}$		$7,9 \times 10^{-12}$	$\langle N_{\epsilon,\text{dyn}} \rangle_{T=100\text{s}}$		$7,9 \times 10^{-12}$
$N_{\text{pol}}^a$	$10^{-5}$	$3,9 \times 10^{-6}$	$N_{\text{pol}}^a$	$10^{-5}$	$5,0 \times 10^{-6}$
$\sigma_{N,\tau=1\text{s}}$	$1,5 \times 10^{-5}$	$9 \times 10^{-8}$	$\sigma_{N,\tau=1\text{s}}$	$1,5 \times 10^{-5}$	$6 \times 10^{-7}$
$\sigma_{N,\delta,\tau=1\text{s}}$	$1,5 \times 10^{-5}$	$10^{-7}$	$\sigma_{N,\delta,\tau=1\text{s}}$	$1,5 \times 10^{-5}$	$6 \times 10^{-7}$
$\sigma_{N,\epsilon,\tau=1\text{s}}$	$3 \times 10^{-6}$	$9 \times 10^{-13}$	$\sigma_{N,\epsilon,\tau=1\text{s}}$	$3 \times 10^{-6}$	$9 \times 10^{-13}$

**Table 1a and b:** theoretical (column 1) and experimental (column 2) nulling budget, spectrally averaged, temporally averaged over 100s (left) or 7h (right).

The intensity mismatch has low impact on the extinction ratio in our set-up because of the high performance of the tip/tilt system. The static part proved to be constant over the spectral band and amounts 0.2%, which is far less than the requirements of 1%. This could be achieved by a fine calibration using the orientation of the PCF at the focus of the collimator. The low tip/tilt noise of 65mas rms results in a very low contribution to the nulling variance. The intensity mismatch has a very low noise well below 0.1% rms.

Thanks to the LQG algorithm, the OPD noise is below 1nm rms (0.74nm rms). Its contribution to the average nulling ratio is limited to  $1.4 \times 10^{-6}$ . The dominant term is the chromatism effect, which reaches  $2.4 \times 10^{-6}$ . It is mainly due to the imperfect realization of the MMZ beam splitters. Fig. 9 shows a simulation of a polychromatic nulling ratio with a  $0.2 \mu\text{m}$  thickness difference between L3a and L4b, superposed with a non uniformity error of the 3 layers coating of variable amplitude (eps is per layer). We know from dedicated measurements that the maximum thickness error is below  $0.28 \mu\text{m}$  considering a set of 9 manufactured beam splitters. This is a pessimistic figure but we don't know the error for the real L3b/L4b pair implemented on the bench.

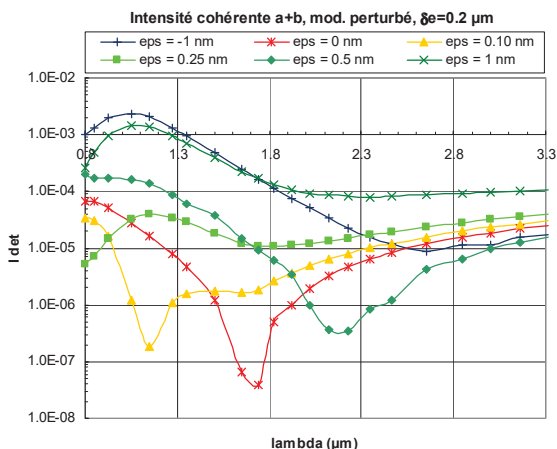


Fig. 9: simulation of the impact of beam splitters defaults on the nulling ratio.

The comparison with the measured data is difficult because the various defaults may combine differently, but a value of eps below 0.25nm, as specified, is coherent with the low chromatism observed between  $1.5 \mu\text{m}$  and  $2.5 \mu\text{m}$ . Both the coating uniformity and the beam splitters thickness have been mastered to an excellent level by the manufacturer.

The polarization effects are only estimated by the complement of the other effects. They are roughly of the same level as the OPD contribution. We cannot separate the rotation effect from the s-p effect. Assuming the rotation effect alone, the obtained static contribution corresponds to a 14 arcmin rotation between arm a and b for one polarization direction. With the s-p effect only, it corresponds to 2.5nm OPD difference of s with respect to p. A dedicated test was performed to estimate the effect of differential angles in the two arms. A variable tilt angle was applied on M1a and the associated correction made on M6a, while the mirrors of the other arms were set to their neutral position. For each value, the OPD was automatically adjusted to minimize the nulling ratio. Fig. 10a and b compare the simulation with the measurement.

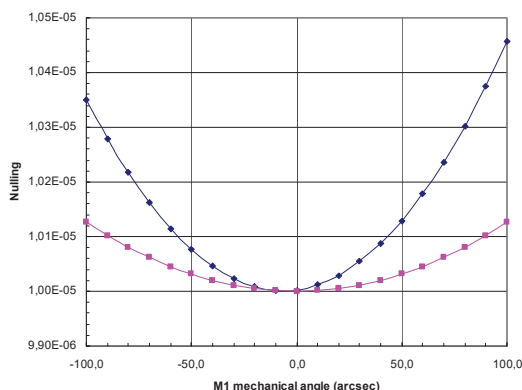


Fig. 10a: monochromatic nulling ratio as a function of M1 tilt, with afocals (blue curve) or not (pink curve).

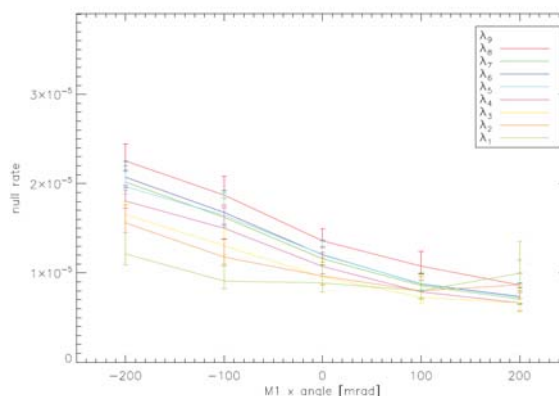


Fig 10b: nulling ratio as a function of M1 tilt, through the 9 spectral bands.

As the law is of quadratic type, a coefficient can be fitted. The theoretical value is  $1.25 \times 10^{-11} \text{ arcsec}^{-2}$  while the experimental one is 4 times greater. This probably comes from the fact that when M1 is tilted, the portion of the associated beam at the output of the collimator moves in a Gaussian shape. The flux mismatch is no longer optimal when M1 moves. Furthermore, this Gaussian shape is not constant with the wavelength because the numerical aperture of the PCF is chromatic. That's why an important chromatic effect can be seen in fig. 10b. A more complicated measurements procedure is planned to disentangle the various effects, but it is not yet implemented. We can nevertheless already conclude that tip/tilt values of up to 200 arcsec of relative misalignment between pairs of mirrors are acceptable for a  $2 \times 10^{-5}$  nulling rate.

### Results over a 7h period under laboratory environment

The measurements were extended to a 7h duration during a night test and results are presented in table 1b. During the test the ambient temperature of the laboratory decreased regularly with a mean slope of  $-13 \mu\text{K/s}$

(from 21.13°C to 20.61°C). As the MMZ and the optics are under a thermal protection, this slope is slightly lower at the MMZ level: -11 μK/s, which translates to -7pm/s on the differential OPD between the FS and the science channel using the coefficient measured previously (see 4.2). The FS calibration is automatically performed every hour resulting in a new interaction matrix between the 8 outputs and the estimated parameters (arms flux in I and J bands, OPD). The tip/tilt and OPD reference points are automatically updated every 100s using a dithering method. This calibration lasts about 30s. Almost all contributors to the nulling budget obtained this way are very close to their value over a 100s period, except one: the bias effect in the reference position of the FS, which is ten times higher and becomes a important contributor. This is because  $\delta_{ref}$  has a mean drift of about 0.6nm between the moment when it is estimated and the next measurement interval of 100s. This shows that long term temperature variations are a limiting factor to nulling measurements over long periods. A much more stable MMZ would be required to avoid too frequent calibrations and loss of precious observation time.

**Results over a 100s with a calibrated disturbance**

The measurements over 100s were repeated with the introduction of the disturbance described in 3.3. Table 2 compares the results obtained with the simple integrator control law and the LQG based one. The disturbance is not well corrected by the integrator. With the LQG control, the measured nulling ratio is only slightly higher than the one measured without the disturbances. This shows the efficiency of the LQG control, if enough flux is available to have the required control bandpass.

Critère	Objectif	Integrateur	LQG
$\sigma_{\delta}$ [nm rms]	1,7	5,57	1,17
$\langle N_{moy} \rangle_{T=100s}$	$10^{-4}$	$8,5 \times 10^{-5}$	$1,14 \times 10^{-5}$
$\langle N_{\delta,w} \rangle_{T=100s}$	$3,5 \times 10^{-5}$	$7,3 \times 10^{-5}$	$3,3 \times 10^{-6}$
$\sigma_{N,\tau=1s}$	$1,5 \times 10^{-5}$	$3 \times 10^{-6}$	$3 \times 10^{-7}$

**Table 2:** nulling ratio over 100s with 18nm rms calibrated disturbance, simple integrator or LQG based

**5. CONCLUSION**

Although our test plan is not yet fully completed, we have reached excellent results with PERSEE. The measured  $10^{-5}$  nulling ratio with a 37% spectral bandwidth and over a 7h duration is a strong support to the feasibility of space based nulling interferometry. The nulling budget is well mastered and all contributors were experimentally estimated. The major contributor is the OPD, which can be controlled to better than 1nm rms. The tip/tilt internal loop with about 1/100 pixel resolution allows a good control of the flux mismatch through the injection into single mode fibers with tip/tilt active mirrors. The maximum correction is about 200 arcsec to avoid the differential polarization effects to become dominant for a  $10^{-5}$  nulling ratio. With such a fine pointing solution in space, the pointing requirements on the spacecrafts would then be directly imposed by the angular magnification and the required nulling ratio. By instance for PEGASE, with M=40 and  $10^{-4}$  nulling, a 10 arcsec classical pointing is compatible with the mission assuming a 400 arcsec stroke, which is not very demanding. With M=200 and  $10^{-5}$  nulling, one would have to constrain the satellite pointing down to the arcsec level or even lower. Our experimental results also prove the efficiency of the spatial filtering using fluoride glass single mode fibers at the  $10^{-5}$  nulling level.

Furthermore, we prove that we can maintain the nulling result despite quite high perturbations levels. Although this was obtained with very high flux, the implemented LQG based method could be helpful for designing an optimal mission and testing it on ground. The measured data can be used to predict the maximal disturbance frequency that can be corrected for a given mission, assuming a list of targets and a set of basic parameters (the diameter of the collector, the optical transmission...). The achromatic  $\pi$ -phase shift using field reversal proved to be very efficient and tolerant to about 100 arcsec differential tip/tilt angles (arm a versus arm b) at the  $10^{-5}$  nulling level. As it allows a simple design reducing the use of additional dispersive elements, this technical solution appears the best for a space based mission. The MMZ based architecture of the combiner is also very efficient. The spatial modulation allows a high bandpass OPD measurement simultaneously with the nulling ratio. This is very important to analyze and correct the OPD effects on the performance, both on ground and in flight. The tight integration of the FS and the science channels reduces the differential thermal drifts. Assuming enough funding for a dedicated thermo-mechanical design with a reduced number of adjustable degrees of freedom, we estimate that this kind of solution can have 60nm/K thermal sensitivity on the differential OPD. Hence a 1nm differential stability could be reached with a temperature stability requirement of about 10mK over a 30cm side box, which seems feasible with standard thermal control techniques, even in non L2 orbits. Last, we developed many calibration and integration procedures, which are very helpful to master such an optical instrument, both on ground and in space.

In the coming year, additional measurements will be made on the bench. First, we will try to acquire and control fringes with initial drifts up to 100 $\mu$ m/s. Then, the source module will be modified to implement a planet and an exo-zodi simulator in order to test various image reconstruction methods.

## 6. REFERENCES

- [1] Léger A. et al., "The DARWIN project", *Astrophysics and Space Science* 241 (1996).
- [2] Léger A. et al., "DARWIN mission proposal to ESA", ESA's Cosmic Vision Call for Proposals (2007).
- [3] Beichman C. A. et al., "The Terrestrial Planet Finder (TPF): a NASA Origins Program to search for habitable planets", *Proc. STSci* (1999).
- [4] Lawson P. R. et al., "Principles of Long Baseline Stellar Interferometry" (2000).
- [5] Danchi W. C. et al., "Scientific rationale for exoplanet characterization from 3-8 microns: the FKSI mission", *Proc. SPIE* 6268 (2006).
- [6] Ollivier M. et al., "Pegase, an infrared interferometer to study stellar environments and low mass companions around nearby stars", ESA's Cosmic Vision Call for Proposals (2007).
- [7] Le Duigou J.M. et al., "Pegase: a space-based nulling interferometer", *Proc. SPIE* 6265 (2006).
- [8] Coudé du Foresto V. et al., "ALADDIN: an optimized nulling ground-based demonstrator for DARWIN", *Proc. SPIE* 6268 (2006).
- [9] Le Duigou J.M. et al., "PERSEE: a nulling breadboard coupled with a free flying GNC simulator", *Proc. SFFMT* (2008).
- [10] Cassaing F. et al., "PERSEE: a nulling demonstrator with real-time correction of external disturbances", *Proc. SPIE* 7013 (2008).
- [11] Houairi K. et al., "PERSEE, the dynamic nulling demonstrator: recent progress on the cophasing system", *Proc. SPIE* (2008).
- [12] Hénault F. et al., "Review of OCA activities on nulling testbench PERSEE", *Proc. SPIE* 7734 (2010).
- [13] Jacquino S. et al., "PERSEE: description of a new concept for nulling interferometry recombination and OPD measurement", *Proc. SPIE* 7013 (2008).
- [14] Serabyn E. et al., "Fully symmetric nulling beam combiners", *Applied Optics* 40 (2001).
- [15] Lozi J. et al., "PERSEE: Experimental results on the cophased nulling bench", *Proc. SPIE* 7734 (2010).
- [16] Lozi J. et al., "Current results of the PERSEE testbench: the cophasing control and the polychromatic null rate", *Proc. SPIE* (2011).
- [17] Villien A. et al., "GNC for the PEGASE mission", *Proc. IFAC* (2007).
- [18] Le Duigou J.M. et al., "Micro vibration measurements on Spot 4, results of the Micromedy experiment", *Spacecraft structures materials and mechanical testing* (1998).
- [19] Serabyn E. et al., "Nulling interferometry: symmetry requirements and experimental results", *Proc. SPIE* 4006 (2010).
- [20] Le Duigou J.M. et al., "First results of the PERSEE Experiment", *Proc. ICSO* (2010).